Enhanced Peltier Effect in Wrinkled Graphene Constriction by Nano-Bubble Engineering

Xudong Hu, Xue Gong, Miao Zhang, Huihui Lu, Zhongying Xue, Yongfeng Mei, Paul K. Chu, Zhenghua An,* and Zengfeng Di*

Inspired by the promising applications in thermopower generation from waste heat and active on-chip cooling, the thermoelectric and electrothermal properties of graphene have been extensively pursued by seeking ingeniously designed structures with thermoelectric conversion capability. The graphene wrinkle is a ubiquitous structure formed inevitably during the synthesis of large-scale graphene films but the corresponding properties for thermoelectric and electrothermal applications are rarely investigated. Here, the electrothermal Peltier effect from the graphene wrinkle fabricated on a germanium substrate is reported. Peltier cooling and heating across the wrinkle are visualized unambiguously with polarities consistent with p-type doping and in accordance with the wrinkle spatial distribution. By direct patterning of the nano-bubble structure, the current density across the wrinkle can be boosted by current crowding to enhance the Peltier effect. The observed Peltier effect can be attributed to the nonequilibrium charge transport by interlayer tunneling across the van der Waals barrier of the graphene wrinkle. The graphene wrinkle in combination with nano-bubble engineering constitutes an innovative and agile platform to design graphene and other more general two-dimensional (2D) thermoelectrics and opens the possibility for realizing active on-chip cooling for 2D nanoelectronics with van der Waals junctions.

1. Introduction

The thermoelectric effect is a physical phenomenon responsible for the conversion to electric voltage by a temperature difference or vice versa, and thermoelectric devices have attracted much interest in energy cycling and thermal management.[1–3] Low-dimensional materials such as two-dimensional (2D) materials and nanowires have emerged as candidates in thermoelectrics due to advantages such as energy quantization resulting from spatial confinement as well as restricted thermal phonon propagation.[4,5] As the most widely studied 2D material, graphene with extraordinary electrical and thermal conductivity has attracted much interest in the thermoelectric field.[6–9] Many studies have focused on the improvement of the thermoelectric performance of graphene by defect engineering[10] or designing nanostructures such as nanomeshes,[11] nanoribbons,[12,13] nanopores,[14] and heterostructures.[15,16] Being the Onsager

Dr. X. Hu, Prof. M. Zhang, Dr. H. Lu, Prof. Z. Xue, Prof. Z. Di
State Key Laboratory of Functional Materials for Informatics
Shanghai Institute of Microsystem and Information Technology
Chinese Academy of Sciences
Shanghai 200050, China
E-mail: zfdi@mail.sim.ac.cn

Dr. X. Hu
University of Chinese Academy of Sciences
Beijing 100049, China

Dr. X. Gong, Prof. Z. An
State Key Laboratory of Surface Physics
Institute for Nanoelectronic Devices and Quantum Computing
Key Laboratory of Micro and Nano Photonics Structures
(Ministry of Education)
Department of Physics
Fudan University
Shanghai 200433, China
E-mail: anzhenghua@fudan.edu.cn

Prof. Y. Mei
Department of Materials Science
Fudan University
Shanghai 200433, China

Prof. P. K. Chu
Department of Physics
Department of Materials Science and Engineering
and Department of Biomedical Engineering
City University of Hong Kong
Tat Chee Avenue, Kowloon, 999077 Hong Kong, China

**ADVANCED
SCIENCE NEWS**
www.advancedsciencenews.com

NANO · MICRO
small
www.small-journal.com

reciprocal of the thermoelectric Seebeck effect, the electro-thermal Peltier effect is also fundamental to thermoelectrics. The Peltier effect often occurs when a current flows through a junction of two dissimilar materials, thus resulting in heating or cooling effects which depend on the current direction. Peltier cooling effect provides an active cooling solution, in contrast to the passive cooling through heat conduction which is limited by thermal conductivity of material itself, and hence has founded important applications in thermoelectric refrigeration. Recently, the Peltier effect has been found to be enhanced when the graphene channel width is reduced to 100 nm, consequently opening the possibility of effective thermal management in graphene electronic devices.[17] Graphene wrinkles exist universally in chemical vapor deposition (CVD) grown graphene films due to the thermal mismatch between graphene and the substrate or subsequent transfer process.[18,19] Unique electrical transport properties have been recently reported by W. Zhu et al. that non-diffusive conductance across graphene wrinkles has weak dependence on the folding length of the wrinkle structures.[18] The observation suggests that graphene wrinkles may also have unique thermoelectric properties including Peltier effects since the electrical conductivity plays a crucial role in the thermoelectric figure-of-merit (ZT). However, the Peltier effect of graphene wrinkles is rarely studied despite the fact that graphene has been considered potentially favorable for solid-state-cooling applications.

In this work, the Peltier effect of graphene wrinkle is observed by scanning thermal microscopy (SThM) for the first time. In combination with highly controllable nano-bubble engineering,[20] the current flowing across the wrinkles can be manipulated and the Peltier effect is found to be enhanced. The effect is attributed to the inter-layer tunneling transport of graphene wrinkles under the intense current density. Our results suggest an innovative approach to realize heat management for graphene electronics and the strategy can be extended to other van-der Waals systems.

2. Results and Discussion

2.1. Peltier Effect in Graphene Wrinkle

SThM is conducted in conjunction with non-equilibrium scanning thermometry to map the temperature difference in the graphene devices (see the Experimental Section).[21,22] As shown in **Figure 1**a, during the SThM measurements, an AC voltage V_{bias} at f_{exc} = 313 Hz is applied to the device metal contacts and as the AC current passes through the graphene channel, the thermoelectric phenomenon including Peltier heating/cooling occurs in addition to Joule heating. The temperature difference is monitored by a SThM tip integrated with a thermocouple at the tip apex as the graphene channel is scanned. The thermal signals are subsequently demodulated by lock-in amplifiers at the second (Joule) harmonic and first (Peltier) harmonic frequencies to extract the Joule heating (Figure 1b) and Peltier heating/cooling (Figure 1c) signals, respectively.

Owing to the thermal expansion mismatch between graphene and Ge, the wrinkles are randomly distributed along a 2 µm wide channel in the graphene device and the device is protected by a hexagonal boron nitride (h-BN) film. The flat h-BN/graphene areas exhibit ultra-low friction as described in previous reports,[23,24] while a clear contrast at the graphene wrinkles can be observed due to friction increase, as marked by the dash dotted lines in lateral friction image (see Figure 1d). For a bias current I of 174 µA which corresponds to the electrical
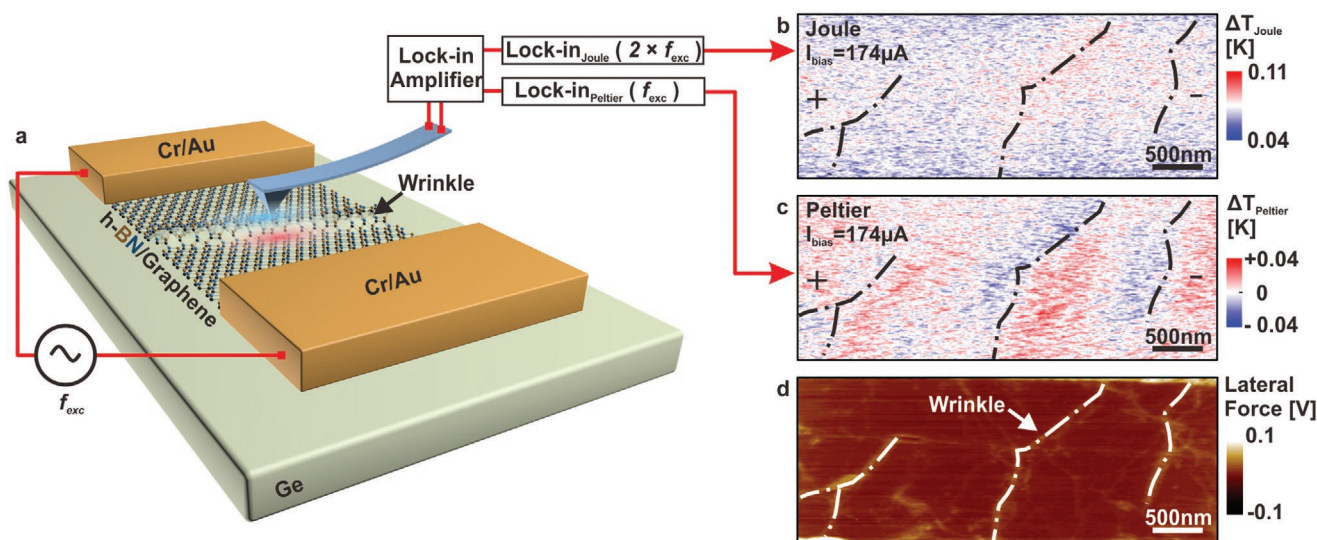

Figure 1. Nanoscale mappings showing Joule effect and Peltier effect of graphene wrinkle on germanium. a) SThM measurements on graphene wrinkle. An AC voltage at f_{exc} applied at metal contacts induces an AC current passing through graphene channel. During SThM scanning, the obtained thermal signals are demodulated by lock-in amplifier to extract Joule heating and Peltier heating/cooling signals. b) Joule heating mapping. c) Peltier effect mapping demonstrates the transition from cooling to heating occurs at graphene wrinkle. d) Lateral friction image of graphene channel for SThM measurement. The positions of wrinkles are marked by dash dotted lines. The polarities of applied voltages are denoted as + and −.

current density of $i \approx 0.3$ µA nm^{-2}, discernable Peltier signals are observed from the graphene wrinkles showing cooling/heating at either side of the wrinkle with $\Delta T_{\text{Peltier}} \cong \pm 0.04$ K (see Figure 1c). The spatial distributions of Peltier signal show excellent correspondence with the wrinkle patterns. Besides, the polarities of the Peltier signals imply that the graphene films are intrinsically p-type[8] consistent with independent characterization performed previously.[25] Meanwhile, the current flowing through the graphene channel produces Joule heating with a peak temperature of $\Delta T_{\text{Joule}} \cong 0.11$ K concentrated at the randomly distributed wrinkles (see Figure 1b).

Although the Peltier effect is observed from the graphene wrinkles, the intensity is too low in practice. Inspired by A. Harzheim's recent work in which the Peltier effect can be significantly enhanced by reducing the graphene channel width,[17] we attempt to improve the weak wrinkle-induced Peltier effect using current crowding by integration of a nano-constriction structure. Nano-patterning by electron beam lithography is an alternative approach to fabricate nano-constriction structure but it is rather challenging to position the randomly distributed wrinkles at the center of the nano-constriction which requires

a sophisticated alignment process. In our study, nano-bubble engineering[20] is utilized to form the nano-constriction structure covering an individual graphene wrinkle precisely.

2.2. Nano-Constriction Fabrication by Nano-Bubble Engineering

In nano-bubble engineering, the graphene nano-bubbles are created at the desired positions on the germanium substrate using a conductive atomic force microscope (AFM) tip. By applying a negative biasing voltage of −6 V to AFM tip with respect to the sample electrodes, hydrogen atoms in Ge–H at the graphene-Ge interface are stimulated into hydrogen molecules to form graphene nano-bubbles.[20] With multiple AFM scans, two stripe-shaped bubbles with the designed sizes and locations are produced and a canyon-like graphene nano-structure is formed, as shown in **Figure 2**a,b. It is well known that the local lattice distortion induced by the nano-bubble structure affects the carrier transport behavior and increases the resistivity of graphene considerably,[26,27] as suggested by the reduced current in the graphene channel after nano-bubble
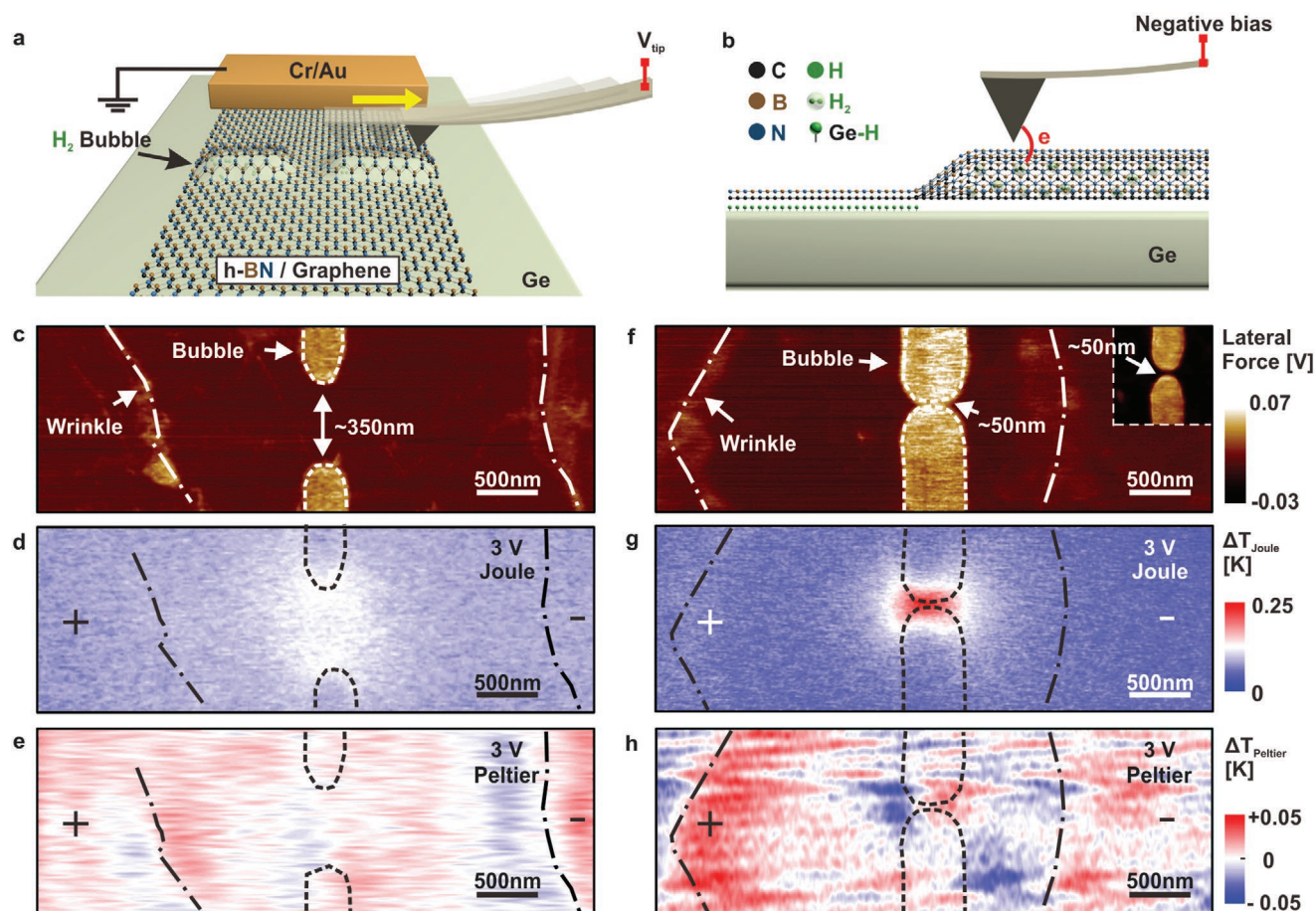

Figure 2. Nanoscale mappings showing Joule effect and Peltier effect of graphene nano-constriction on germanium. a) Schematic illustration of nano-bubble engineering for graphene nano-constriction fabrication. b) Zoom-in schematic of stimulating h-BN/Graphene nano-bubble on germanium. c–e) The lateral friction, Joule heating, and Peltier heating/cooling images of graphene nano-constriction with ≈350 nm channel width. f–h) The lateral friction, Joule heating and Peltier heating/cooling images of graphene nano-constriction with ≈50 nm channel width. The inset in (f) presents a clear image of nano-constriction channel using a special tip with 2–12 nm radius. The contours of graphene bubbles are outlined by densely dashed lines, and the positions of wrinkles are marked by dash-dotted lines. The polarities of applied voltages are denoted as + and −.

fabrication (see Figure S1, Supporting Information). Therefore, analogous to the removal of the partial channel area to form the nano-constriction structure by electron beam lithography, nano-bubble engineering is used to increase the local resistivity of the graphene bubble region to create the nano-constriction structure. Meanwhile, nano-constriction can be precisely designed at the desired location on account of the high precision of AFM. By tuning the distance between two stripe-shaped bubbles, nano-constriction with a controllable size can be formed in the channel region of the graphene device as shown in Figure 2c,f. Since the channel region is initially covered by the h-BN film for protection, the subsequent graphene nano-bubbles are protected by h-BN as well. As shown in Figure 2c,f, the friction at the h-BN/graphene bubble region is considerably higher than that on the flat h-BN/graphene areas consistent with the previous reports.[23,24] According to the large friction contrast, the width (W) of the graphene nano-constriction can be distinguished and two typical examples with W of 350 and 50 nm are shown in Figure 2c,f, respectively. For a typical bias V_{bias} of 3 V, the electrical currents of the two typical samples are 168 µA ($W \approx 350$ nm) and 152 µA ($W \approx 50$ nm), corresponding to electrical current densities of $i \approx 1.4$ and 8.7 µA nm^{-2}, respectively. The current densities readily exceed the reported breakdown current density value for layer-transferred graphene on SiO$_2$ (≈ 1 µA nm^{-2}) and are more than two orders higher than the fundamental electromigration limit for metals.[28] The high current densities produce remarkable Joule heating producing hot spots as shown in Figure 2d (peak temperature of $\Delta T_{Joule} \cong 0.14$ K) and **g** ($\Delta T_{Joule} \cong 0.25$ K). The hot spot exhibits an elongated shape perpendicular to the channel direction for the nano-constriction with W of 350 nm (Figure 2d) but parallel to the channel direction for $W \approx 50$ nm (Figure 2g), implying different local current distributions. Meanwhile, the constricted channels produce discernible Peltier signals as demonstrated in Figure 2e ($\Delta T_{Peltier} \cong \pm 0.01$ K) and **h** ($\Delta T_{Peltier} \cong \pm 0.05$ K).

The amplitudes of the Peltier effects observed from the graphene nano-constrictions are comparable to that of the graphene wrinkles. The wrinkles (dash dotted lines in Figure 2c,f) away from the constricted-channel region also show the Peltier signals ($\Delta T_{Peltier} \cong \pm 0.01 - 0.05$K), which agrees with the results in Figure 1 and verifies the generality of the Peltier effects in graphene wrinkles. The absolute amplitude of the Peltier signal from the graphene wrinkle appears to have the same magnitude as that of the graphene nano-constriction. However, considering that the current density in the constricted channel is substantially higher (i.e., current crowding) while the current density across the wrinkles is dispersed considerably ($i \approx 0.2$ µA nm^{-2} for wrinkles versus $i \approx 1.4$ µA nm^{-2} for the 350 nm constriction channel in Figure 2c; $i \approx 0.2$ µA nm^{-2} for wrinkles versus 8.7 µA nm^{-2} for the 50 nm constriction channel in Figure 2f), the graphene wrinkle should be more sensitive than graphene nano-constriction in terms of the Peltier effect. Therefore, the Peltier effect of the graphene wrinkle is expected to be enhanced if the flowing current density is boosted intentionally by placing the graphene wrinkle in the nano-constriction structure and it will be discussed later. Considering the proportional relationship of Peltier effect on current density,[17] the current-carrying capacity of graphene device is essential for the improvement of Peltier effect by increasing

current density. In typical graphene device on SiO$_2$/Si substrate, the current density is suppressed by the low thermal conductivity of SiO$_2$ $K = 0.5–1.4$ W m^{-1} K^{-1} at RT.[28] In our graphene/Ge system, the current-carrying capacity is enhanced due to the much higher thermal conductivity of Ge $K \approx 60$ W m^{-1} K^{-1},[29] as well as good thermal contact between CVD-grown graphene and the substrate, which substantially increases the breakdown current density of graphene channel. Similar increased current-carrying capacity (≈ 18 µA nm^{-2}) is also reported for graphene-on-diamond devices.[28] Besides, it is noteworthy to mention that Figure 2d,g show no obvious Joule heating signals from the graphene wrinkles suggesting that the graphene wrinkles produce far less Joule heat than the confined nano-channels boding well for graphene thermoelectrics.

2.3. Peltier Effect in the Graphene Wrinkle within Nano-Constriction

In order to intentionally increase the current density through the graphene wrinkle, one stripe-shaped bubble is fabricated to cater to an individual graphene wrinkle by taking advantage of the high accuracy of AFM. This process produces the graphene nano-constriction with a single wrinkle embedded as shown in **Figure 3**a,b. Figure 3c to h display Joule heating (c, e, g) and Peltier heating/cooling (d, f, h) at the wrinkle embedded in the graphene nano-constriction as the AC voltage is increased gradually. Both the Joule and Peltier signals increase monotonously when the voltage is increased from 1 to 3 V. When applying an AC voltage of 3 V with current $I_{bias} \approx 107$ µA (or $i \approx 0.8$ µA nm^{-2}), the Peltier effect results in cooling and heating effects up to $\Delta T_{Peltier} \approx -0.226$ K/+0.157 K, which is significantly larger than that observed from the graphene wrinkle away from the constricted channel shown in Figures 1 and 2. The slight asymmetry between Peltier cooling and heating may arise from the asymmetry of the whole device (see Figure S2, Supporting Information). The intensity of the Peltier heating/cooling signal is comparable to the peak value of Joule heating which is up to $\Delta T_{Joule} \approx 0.374$ K. When the bias applied to the two-terminal electrodes is reversed, the Peltier heating and cooling signal is reversed correspondingly, while the peak position for Joule heating signal remains steady except a slight change in the contour shape, as depicted in Figure 3i,j. The observed difference ascertains the current-direction dependent nature of the Peltier effect as well as independence of the Joule effect on the current direction. In addition, the hot spot for Joule heating appears at a position coinciding with the narrowest point of the nano-constriction, while the transient boundary for Peltier cooling/heating always emerges from the wrinkle position regardless of the current direction, as indicated by the dash dotted line in Figure 3. This tendency agrees with the results in Figure 2 implying that the Joule effect is closely related to the geometry of the nano-constriction due to the variation in the current density, whereas the Peltier effect is mainly determined by the graphene wrinkle. Besides the current density, the dimension of the graphene wrinkle alters the Peltier effect that is reduced considerably for small graphene wrinkle as shown in Figure S3, Supporting Information. The Peltier signals are also found from the graphene wrinkle embedded by traditional geometrical
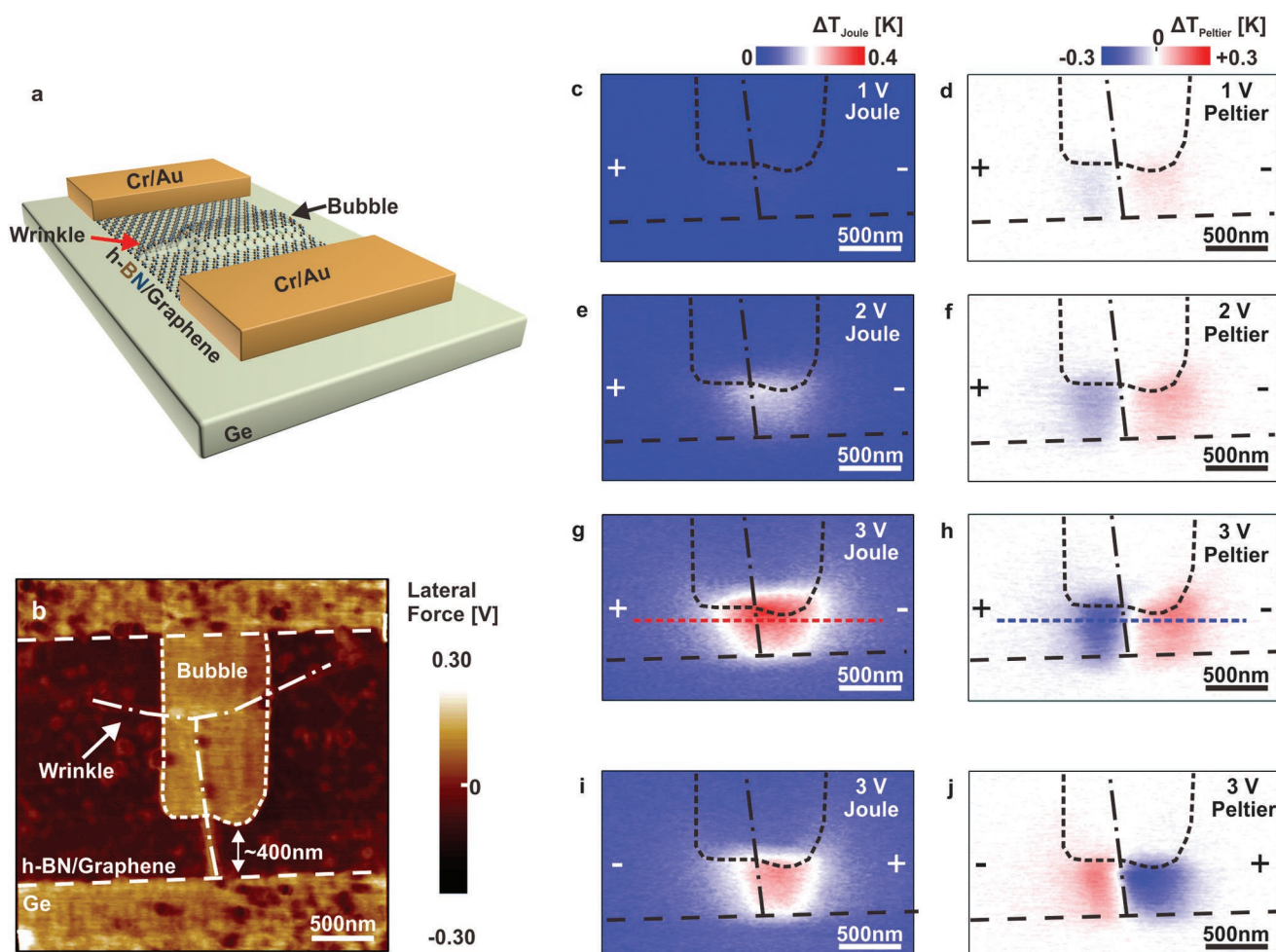
ADVANCED
SCIENCE NEWS
www.advancedsciencenews.com

NANO · MICRO
small
www.small-journal.com

Figure 3. Nanoscale mappings showing Joule effect and Peltier effect of graphene wrinkle embedded in nano-constriction on germanium. a) Schematic illustration of graphene wrinkle embedded in nano-constriction. b) Lateral friction image of graphene wrinkle embedded in nano-constriction. The dashed lines show two edges of graphene channel on germanium, the densely dashed line outlines the contour of graphene bubbles, and the dash-dotted line marks the position of graphene wrinkle. An individual graphene wrinkle is embedded in nano-constriction with the width of $\approx$400 nm. c–h) The evolution of Peltier heating/cooling and Joule heating effects in graphene wrinkle embedded in nano-constriction at the AC voltages varying from 1 to 3 V. i,j) Peltier heating/cooling and Joule heating mappings at 3 V with the reversed bias applied at two-terminal electrodes. The polarities of applied voltages are denoted as + and −.

confinement using electron beam lithography despite the sophisticated process and limited alignment accuracy (Figure S4, Supporting Information). The similar Peltier effect shown in Figure S4, Supporting Information, not only demonstrates the equivalence of the nano-bubbling engineering technique, but also verifies the general validity of the unique thermoelectric properties of graphene wrinkles. Our nano-bubble engineering technique provides a simpler approach to fabricate constriction channel as no any chemical resist is needed, and the fabricated conductive graphene channel can be as narrow as sub-20 nm, similar to the reported performance by AFM lithography technique.[30]

Both the Joule and Peltier effects in the graphene wrinkle embedded in the nano-constriction are investigated in detail as shown in **Figure 4**. Figure 4a,b shows the line profiles of Joule heating and Peltier heating/cooling along the current direction (marked by horizontal short-dashed lines in Figure 3g,h, respectively) at various AC voltages (up to 3 V). The vertical black dotted lines in Figure 4a,b indicate the identical position of the same wrinkle embedded in the nano-constriction ($x = 0$). With regard to the Joule heating effect (Figure 4a), the intensity distributions of Joule heating can be fitted by the symmetric Gaussian function. The maximum peaks of the temperatures deviate from the location of the graphene wrinkle ($x \cong 0.1 \ \mu m$) but coincide with the narrowest point of the constriction channel. For the Peltier effect (Figure 4b), the signals have an approximately anti-symmetric line-shape and the position of the wrinkle emerges at the transition position between the heating and cooling signals. Therefore, the discrepancy between the hot spots of Joule heating and transition boundary of Peltier heating/cooling exists and it is consistent with the results in Figure 3. The observed phenomenon has an important implication that the Peltier and Joule effects can be decoupled and the Peltier effect observed from the graphene wrinkle is promising in thermoelectric materials with limited Joule heating.
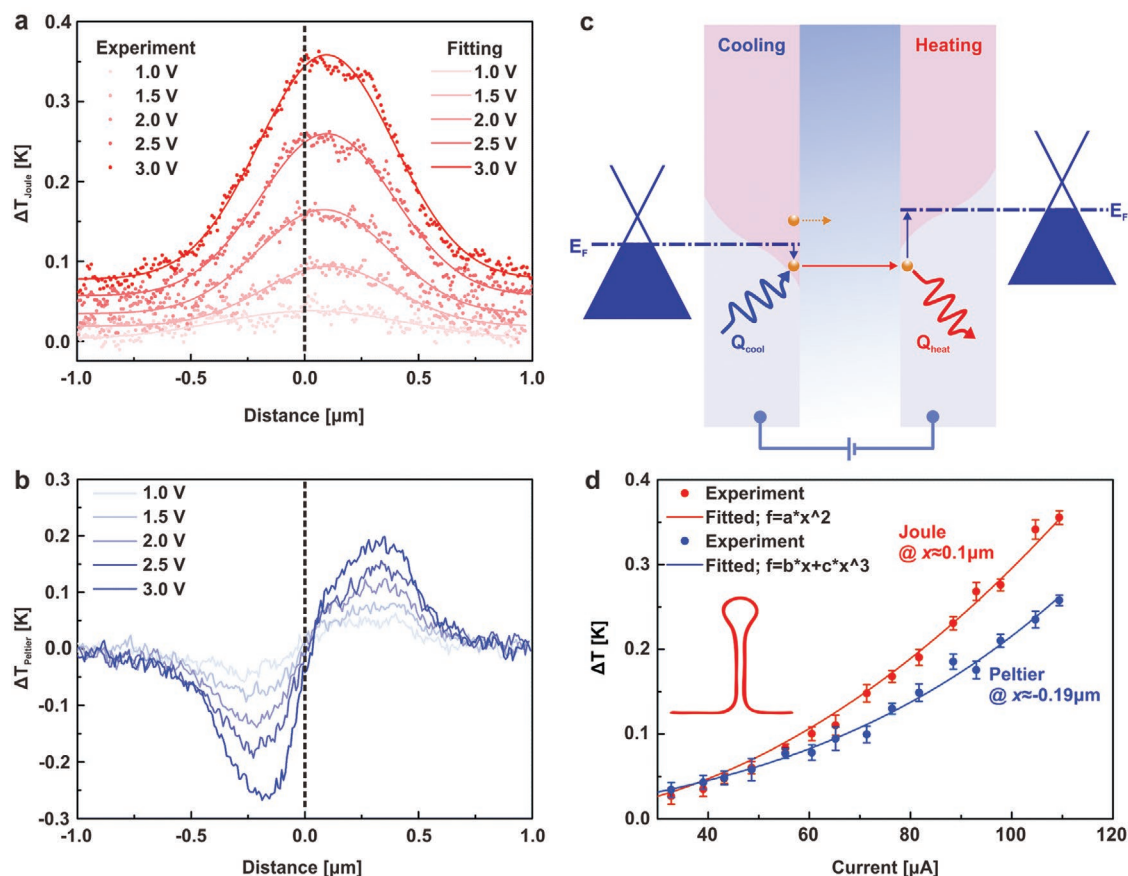
Figure 4. Numerical analysis of Peltier effect and Joule effect of graphene wrinkle embedded in nano-constriction on germanium. a,b) Line-scan profiles of Joule and Peltier signals in nano-constriction at different applied AC voltages (extracted from the red short-dashed line in Figure 3g and blue short-dashed line in Figure 3h). The vertical black dotted lines indicate the same position of wrinkle. c) Schematic illustration of physical mechanism underlying Peltier heating/cooling process at graphene wrinkle. d) Current dependence of the maximum Joule heating ($x \approx 0.1\,\mu m$) and the maximum Peltier cooling ($x \approx -0.19\,\mu m$). The maximum Joule heating has a quadratic current dependence, while the maximum Peltier cooling is well fitted by the sum of linear and cubic order terms. The inset in (d) shows the schematic of a typical wrinkle.

The current dependence of Joule heating and Peltier cooling is summarized in Figure 4d. For Joule heating measurements performed at hot spot corresponding to the peak position ($x \cong 0.1\,\mu m$), a quadratic dependence of Joule heating on the current is observed and agrees with the Joule–Lenz law ($P \propto I^2R$). In the Peltier measurements, the maximum cooling ($x \cong -0.19\,\mu m$) shows a continuous change in the current dependence from the linear to cubic correlation as the current is increased gradually (Figure 4d). The deviation from the linear dependence $\dot{Q} = \Pi * I_{bias} = ST * I_{bias}$ is also observed by Harzheim.[17] The deviation is attributed to the so-called "electron wind" effect[17] or essentially quasi-ballistic transport[31] if the drift velocity of the carriers becomes comparable to the Fermi velocity. Consequently, heat is inclined to shift with respect to the position of the wrinkle and the cooling and heating phenomena appear from either side of the graphene wrinkle depending on the direction of current.[17]

The Peltier effect observed from the graphene wrinkle can be ascribed to the charge tunneling transport across the graphene wrinkle. In the graphene wrinkle, the layers are folded at the wrinkle position[18] and form a van der Waals junction, as schematically shown in the inset in Figure 4c. For simplicity,

we only consider the standing wrinkle structure here, but our scenario remains valid for other possible wrinkle structures as discussed in ref. [18]. The inter-layer tunneling charge transport across the van der Waals junction dominates and compensates for the increased graphene length due to folding and as a result, the net conductance remains nearly unchanged,[18] which is in good agreement with the experimental finding that no remarkable Joule heat is detected from the wrinkles. In terms of the Peltier effect, previous reports[8,31–33] show that the potential barrier provides an energy filtering effect for the nonequilibrium transportation of charge carriers. Here, the van der Waals tunneling barrier originating from the graphene wrinkle plays a crucial role in the Peltier effect, as schematically shown in Figure 4c. Different from ref. [32], the graphene film is p-type in this work and the majority carriers are holes (see the Experimental Section). The holes tunnel from the left (source) side to the right (drain) one through the interlayer barrier. The holes at the source side are initially in nearly thermal equilibrium with the lattice and the distribution is a Fermi–Dirac function at temperature T ($T_{hole} \approx T_{lattice}$). Based on this distribution, only the holes with the forward momentum and energy larger than the barrier can tunnel through the barrier. Since some of the

holes at the high energy tail of the distribution are able to leave, the remaining holes have an average energy below $3/2k_BT$ (k_B is the Boltzmann constant). By the principle of balance, these holes absorb more phonons during dynamic thermalization with the lattice eventually contributing to Peltier cooling of the lattice on the left side. Accordingly, the holes tunneling into the right side are in thermal non-equilibrium ($T_{hole} > T_{lattice}$) and cause Peltier heating. In this charge tunneling transport process, the negligible thickness of the van der Waals tunnel junction enables elastic tunneling with the prominent Peltier effect but little Joule heat simultaneously. It is analogous to the energy barrier in heterojunction laser diodes introduced by band structure offsets and optimized to provide internal thermoelectric cooling near the active laser region.[34]

The structure of graphene wrinkle affects the carrier transport[18] as well as the induced Peltier effect, which has been shown in Figure 3 and Figure S3, Supporting Information. Considering that the Peltier effect is caused by carrier elastic tunneling across the graphene interlayer, the Peltier effect is expected to be optimized by maximizing the contribution of tunneling current through wrinkle, which means that folded wrinkles are preferred. In graphene wrinkle with folded structure, the current mainly flows between graphene layers at the base of wrinkle rather than through the whole length,[18] thus resulting in maximized tunneling transport and optimized Peltier effect. For the practical application of Peltier effect from wrinkle, it is significant to form wrinkle controllably with specific structure and desired position. As previously reported by Z. Pan et al.[35] and by T. Chen et al.,[36] wrinkle engineering has been realized and shown its capability in controlling the dimension, density, position, and orientation of wrinkles on transferred CVD-graphene, which can be applied to fabricate graphene wrinkle with desired structure. Exploiting the wrinkle engineering technique[35,36] in conjunction with high-resolution patterning of nano-bubble engineering, arrays of wrinkled graphene device can be fabricated in the controllable manner for large-scale Peltier application. In fact, narrow graphene bubble stripes, which can be considered as artificial graphene wrinkle with the similar dimension, have exhibited the potential in extending the Peltier effect to larger-scale via array patterning (see Figure S5, Supporting Information).

As the scaling down of electronic devices, larger power densities are generated in integrated circuits, causing local hot spots. The high heat fluxes of these hot spots make the passive cooling insufficient to maintain the performance and reliability of integrated circuits.[9] It is known that a combination of effective passive cooling and active cooling is often utilized to address the long-lasting electronic cooling issue.[37] Due to the excellent thermal conductivity of graphene, the passive cooling operating via the phonon channel is rather efficient in graphene-based devices. However, the active cooling utilizes the Peltier cooling to pump the thermal heat through the electronic channel, and it is easily affected by the surroundings. J. Duan et al. reported that the Peltier effect of graphene can be significantly improved by using hexagonal boron nitride (h-BN) substrates instead of SiO$_2$ due to the reduced potential fluctuations and higher carrier mobility in graphene/h-BN.[9] In addition, the pronounced Peltier effect is also found in 100 nm wide graphene bow-tie nanoconstrictions, in which the edge scattering becomes more dominant

as the width of nanoconstriction shrinks.[17] Our work suggests that, in conjunction with the nanoconstriction created by nano-bubble engineering, graphene wrinkle can be utilized for the active cooling purpose, which can be further explored for the local thermal management in future graphene nanoelectronics.

3. Conclusion

In summary, Peltier cooling and heating across graphene wrinkles on germanium are observed during current flow. In conjunction with nano-bubble engineering, the Peltier effect can be remarkably enhanced due to current crowding without substantial increase of Joule heating. The unique thermoelectric property of graphene wrinkle can be attributed to the hot hole transport through interlayer elastic tunneling across the van der Waals barrier of the graphene wrinkles. Our results reveal a versatile platform to realize heat management in graphene electronics and provide insights into the design of thermoelectrics with van der Waals junctions composed of 2D materials.

4. Experimental Section

Device Fabrication: The single-crystal graphene films were prepared directly on (110) germanium by CVD.[25,38,39] The graphene film is often p-type as reported previously.[25] Direct Terahertz time-domain spectrometry conducted on graphene/germanium showed a 2D sheet carrier density of 3×10^{12} cm^{-2} and mobility of 1×10^4 cm^2 V^{-1} S^{-1} following the method introduced by J. D. Buron et al.[40] The Cr/Au contacts were deposited onto graphene by shadow masking using electron-beam evaporation. Subsequently, the graphene channel was patterned by lithography and etched by reactive ion etching with oxygen. The graphene channels were designed to be 2 μm wide and 10 μm long. The single-layer h-BN films prepared on copper foils were transferred to the graphene devices for protection using a standard wet transfer method.[41,42]

Nano-Bubble Engineering: The detailed process for nano-bubble creation can be found in ref. [20]. During the formation of nano-bubbles, the Cr/Au contact in the device was grounded and the bias V_{tip} on the conducting AFM tip was −6 V during scanning of the selected area of the graphene channel covered by h-BN. The AFM system used in nano-bubble engineering is Bruker Dimension Icon, and the conducting AFM tip used here is Pt/Ir coated silicon tip (ANSCM-PC, APPNANO) with radius of curvature ≈30 nm. Our nano-bubble engineering technique can be applied in a wide range of 2D materials if hydrogen atoms can be intentionally introduced between the 2D film and the substrate, for example, hydrogenation of the substrate in acid solution prior to the layer transfer process.

Scanning Thermal Microscopy: A passive SThM system was used to study the Joule effect and Peltier effect. The apparatus was placed in the ambient environment and the spatial resolution was determined by the tip size of the thermocouple (about 50 nm). In the Peltier measurement, the device was subjected to an AC voltage V_{bias} through the Cr/Au contacts at a frequency of $f_{exc} = 313$ Hz. During the SThM measurement, the thermal signals collected by the tip were sent to VertiSense imaging amplifier and demodulated by a SRS830 lock-in amplifier. The Peltier signal $\Delta T_{Peltier}$ was demodulated at the first harmonic (f) and the Joule heating signal ΔT_{Joule} was demodulated at the second harmonic (2f). The Peltier and Joule measurements were performed following the method introduced by Harzheim[17] and Menges[22] to exclude the tip-sample and contact-related artifacts. In addition, the Peltier and Joule measurement channels were tuned to have the same temperature sensitivity in order to ensure that the measured temperatures could be compared directly.

Supporting Information

Supporting Information is available from the Wiley Online Library or from the author.

Acknowledgements

Conflict of Interest

The authors declare no conflict of interest.

Keywords

[1] B. Poudel, Q. Hao, Y. Ma, Y. Lan, A. Minnich, B. Yu, X. Yan, D. Wang, A. Muto, D. Vashaee, X. Chen, J. Liu, M. S. Dresselhaus, G. Chen, Z. Ren, *Science* **2008**, *320*, 634.

[2] L.-D. Zhao, S.-H. Lo, Y. Zhang, H. Sun, G. Tan, C. Uher, C. Wolverton, V. P. Dravid, M. G. Kanatzidis, *Nature* **2014**, *508*, 373.

[3] F. J. DiSalvo, *Science* **1999**, *285*, 703.

[4] L. D. Hicks, M. S. Dresselhaus, *Phys. Rev. B* **1993**, *47*, 12727.

[5] L. D. Hicks, M. S. Dresselhaus, *Phys. Rev. B* **1993**, *47*, 16631.

[6] K. L. Grosse, M.-H. Bae, F. Lian, E. Pop, W. P. King, *Nat. Nanotechnol.* **2011**, *6*, 287.

[7] X. Xu, N. M. Gabor, J. S. Alden, A. M. Van Der Zande, P. L. McEuen, *Nano Lett.* **2010**, *10*, 562.

[8] I. J. Vera-Marun, J. J. van den Berg, F. K. Dejene, B. J. van Wees, *Nat. Commun.* **2016**, *7*, 11525.

[9] J. Duan, X. Wang, X. Lai, G. Li, K. Watanabe, T. Taniguchi, M. Zebarjadi, E. Y. Andrei, *Proc. Natl. Acad. Sci. U. S. A.* **2016**, *113*, 14272.

[10] Y. Anno, Y. Imakita, K. Takei, S. Akita, T. Arie, *2D Mater.* **2017**, *4*, 025019.

[11] J. Oh, H. Yoo, J. Choi, J. Y. Kim, D. S. Lee, M. J. Kim, J. C. Lee, W. N. Kim, J. C. Grossman, J. H. Park, S. S. Lee, H. Kim, J. G. Son, *Nano Energy* **2017**, *35*, 26.

[12] Y. Ouyang, J. Guo, *Appl. Phys. Lett.* **2009**, *94*, 263107.

[13] Q. Y. Li, T. Feng, W. Okita, Y. Komori, H. Suzuki, T. Kato, T. Kaneko, T. Ikuta, X. Ruan, K. Takahashi, *ACS Nano* **2019**, *13*, 9182.

[14] P. H. Chang, B. K. Nikolić, *Phys. Rev. B* **2012**, *86*, 041406.

[15] Y. Yokomizo, J. Nakamura, *Appl. Phys. Lett.* **2013**, *103*, 113901.

[16] C. C. Chen, Z. Li, L. Shi, S. B. Cronin, *Nano Res.* **2015**, *8*, 666.

[17] A. Harzheim, J. Spiece, C. Evangeli, E. McCann, V. Falko, Y. Sheng, J. H. Warner G. A. D. Briggs, J. A. Mol, P. Gehring, O. V. Kolosov, *Nano Lett.* **2018**, *18*, 7719.

[18] W. Zhu, T. Low, V. Perebeinos, A. A. Bol, Y. Zhu, H. Yan, J. Tersoff, P. Avouris, *Nano Lett.* **2012**, *12*, 3431.

[19] L. Lin, B. Deng, J. Sun, H. Peng, Z. Liu, *Chem. Rev.* **2018**, *118*, 9281.

[20] P. Jia, W. Chen, J. Qiao, M. Zhang, X. Zheng, Z. Xue, R. Liang, C. Tian, L. He, Z. Di, X. Wang, *Nat. Commun.* **2019**, *10*, 3127.

[21] R. J. Qian, X. Gong, H. Y. Xue, W. K. Lu, L. P. Zhu, Z. H. An, *ES Energy Environ* **2019**, *6*, 4.

[22] F. Menges, P. Mensch, H. Schmid, H. Riel, A. Stemmer, B. Gotsmann, *Nat. Commun.* **2016**, *7*, 10874.

[23] C. Lee, Q. Li, W. Kalb, X. Z. Liu, H. Berger, R. W. Carpick, J. Hone, *Science* **2010**, *328*, 76.

[24] X. Zheng, L. Gao, Q. Yao, Q. Li, M. Zhang, X. Xie, S. Qiao, G. Wang, T. Ma, Z. Di, J. Luo, X. Wang, *Nat. Commun.* **2016**, *7*, 13204.

[25] G. Wang, M. Zhang, Y. Zhu, G. Ding, D. Jiang, Q. Guo, S. Liu, X. Xie, P. K. Chu, Z. Di, X. Wang, *Sci. Rep.* **2013**, *3*, 2465.

[26] X. W. Fu, Z. M. Liao, J. X. Zhou, Y. B. Zhou, H. C. Wu, R. Zhang, G. Jing, J. Xu, X. Wu, W. Guo, D. Yu, *Appl. Phys. Lett.* **2011**, *99*, 213107.

[27] N. Leconte, H. Kim, H. J. Kim, D. H. Ha, K. Watanabe, T. Taniguchi, J. Jung, S. Jung, *Nanoscale* **2017**, *9*, 6041.

[28] J. Yu, G. Liu, A. V. Sumant, V. Goyal, A. A. Balandin, *Nano Lett.* **2012**, *12*, 1603.

[29] R. Jalilian, G. U. Sumanasekera, H. Chandrasekharan, M. K. Sunkara, *Phys. Rev. B* **2006**, *74*, 155421.

[30] I. S. Byun, D. Yoon, J. S. Choi, I. Hwang, D. H. Lee, M. J. Lee, T. Kawai, Y. W. Son, Q. Jia, H. Cheong, B. H. Park, *ACS Nano* **2011**, *5*, 6417.

[31] Q. Weng, S. Komiyama, L. Yang, Z. An, P. Chen, S-A. Biehs, Y. Kajihara, W. Lu, *Science* **2018**, *360*, 775.

[32] L. Cui, R. Miao, K. Wang, D. Thompson, L. A. Zotti, J. C. Cuevas, E. Mayhofer, P. Reddy, *Nat. Nanotechnol.* **2018**, *13*, 122.

[33] M. G. Rosul, D. Lee, D. H. Olson, N. Liu, X. Wang, P. E. Hopkins, K. Lee, M. Zebarjadi, *Sci. Adv.* **2019**, *5*, eaax7827.

[34] K. P. Pipe, R. J. Ram, A. Shakouri, *IEEE Photonics Technol. Lett.* **2002**, *14*, 453.

[35] Z. Pan, N. Liu, L. Fu, Z. Liu, *J. Am. Chem. Soc.* **2011**, *133*, 17578.

[36] T. Chen, Y. Xue, A. K. Roy, L. Dai, *ACS Nano* **2014**, *8*, 1039.

[37] G. J. Snyder, E. S. Toberer, C T Materials. *Nat. Mater.* **2008**, *7*, 105.

[38] J. H. Lee, E. K. Lee, W. J. Joo, Y. Jang, B. S. Kim, J. Y. Lim, S. H. Choi, S. J. Ahn, J. R. Ahn, M. H. Park, C. W. Yang, B. L. Choi, S. W. Hwang, D. Whang, *Science* **2014**, *344*, 286.

[39] J. Dai, D. Wang, M. Zhang, T. Niu, A. Li, M. Ye, S. Qiao, G. Ding, X. Xie, Y. Wang, P. K. Chu, Q. Yuan, Z. Di, X. Wang, F. Ding, B. I. Yakobson, *Nano Lett.* **2016**, *16*, 3160.

[40] J. D. Buron, D. M. A. Mackenzie, D. H. Petersen, A. Pesquera, A. Centeno, P. Bøggild, A. Zurutuza, P. U. Jepsen, *Opt. Express* **2015**, *23*, 30721.

[41] X. Li, W. Cai, J. An, S. Kim, J. Nah, D. Yang, R. Piner, A. Velamakanni, I. Jung, E. Tutuc, S. K. Banerjee, L. Colombo, R. S. Ruoff, *Science* **2009**, *324*, 1312.

[42] J. W. Suk, A. Kitt, C. W. Magnuson, Y. Hao, S. Ahmed, J. An, A. K. Swan, B. B. Goldberg, R. S. Ruoff, *ACS Nano* **2011**, *5*, 6916.